Chondrule flattening by shock metamorphism in unequilibrated chondrites

Masaaki Miyahara[1*], Junnosuke Edanaga[1], Akira Yamaguchi[2], Takamichi Kobayashi[3], Toshimori Sekine[4,5], and Ayaka Nakamura[1]

[1]Graduate School of Advanced Science and Engineering, Hiroshima University, Higashi-Hiroshima, 739-8526, Japan
[2]National Institute of Polar Research, Tokyo 190-8518, Japan
[3]National Institute for Materials Science, Tsukuba 305-0047, Japan
[4]Center for High Pressure Science and Technology Advanced Research, Pudong, Shanghai 201203, P.R. China
[5]Graduate School of Engineering, Osaka University, Suita, Osaka 565-0871 Japan

*Corresponding author: Dr. Masaaki Miyahara
Graduate School of Advanced Science and Engineering, Hiroshima University, Higashi-Hiroshima, 739-8526, Japan.
Postal code: 739-8526
Telephone: +81-824-24-7461
FAX: +81-82-424-0735
E-mail address: miyahara@hiroshima-u.ac.jp

Key points:

- Shock experiments of H/L3 chondrites were conducted in the range of 11–43 GPa.
- Shock-induced melting occurs above 11 GPa and the aspect ratios of chondrules increase with increasing shock pressure.
- No differences in chondrule flattening between carbonaceous and ordinary chondrites.

Abstract

Shock recovery experiments using ALH-78084 H3 and Y-793375 L3 chondrites are conducted in the shock pressure range of 11–43 GPa to reproduce shock-induced melting and chondrule flattening. Shock experiments prove that shock-induced melting occurs beyond 11 GPa at least. The melting occurs at the boundaries between chondrules and matrices. The melts include fine-grained silicate minerals,

glasses, and amoeba or spherical metallic Fe-Ni or metallic Fe-Ni–iron-sulfide with a eutectic texture, which coincides with shock-induced melts in shocked natural chondrites. Shock experiments also prove that shock-induced flattening of chondrules occurs and the flattening degree increases with increasing shock pressure. Taking account of not only the shock experiments of ordinary chondrites but also carbonaceous chondrites, the flattening degree does not depend significantly on the densities, porosities, and chondrule/matrix ratios of chondrites. Considering the shock experiments of the Allende CV3 and Murchison CM2 carbonaceous chondrites along with present shock experiments using H/L3 ordinary chondrites, the aspect ratios of chondrules in unequilibrated chondrites (R_{cho}) can be expressed as follows: R_{cho} = 0.011 (±1) × Pressure (GPa) + 1.18 (±3). The long axes of chondrules in shocked ALH-78084 H3 and Y-793375 L3 chondrites have preferred orientations and the degree increases with increasing shock pressure. Natural L/LL3 ordinary chondrites with shock-induced melts have higher aspect ratios and preferred orientations than those without shock-induced melts although it is difficult to determine quantitatively shock pressure using the empirical formula between the aspect ratios of chondrules and shock pressure.

Plain Language Summary

An early ordinary chondrite parent-body had an onion-shell structure and was disrupted by an impact. Some ordinary chondrites derived from the parent-body surface have melts, high-pressure polymorphs, and flattened chondrules, which may be due to shock metamorphism. Hence, shock recovery experiments using ordinary chondrites were conducted in the shock pressure range of 11–43 GPa to reproduce shock-induced melting and chondrule flattening. Shock-induced melting occurs beyond 11 GPa. The melting occurs at a boundary between chondrules and surrounding fine-grained materials. Shock-induced flattening of chondrules occurs and the flattening degree increases with increasing shock pressure. Taking account of not only the shock experiments of ordinary chondrites but also carbonaceous chondrites, the flattening degree does not depend significantly on the densities, porosities, and chondrule/matrix ratios of chondrites. The aspect ratios of chondrules in unequilibrated chondrites (Rcho) can be expressed as follows: Rcho = 0.011 (±1) × Pressure (GPa) + 1.18 (±3). The long axes of chondrules in experimentally shocked ordinary chondrites have preferred orientations and the degree increases with increasing shock pressure.

1. Introduction

One of the classic structure models for ordinary chondrite parent-bodies is the onion shell model derived from maximum metamorphic temperature and cooling rate recorded in each petrologic type ordinary chondrite (e.g., Trieloff et al., 2003). Following the onion shell model, early ordinary chondrite parent-bodies had consisted of petrologic type 3–6 ordinary chondrites toward the inside from the outside. The early ordinary chondrite parent-bodies were disrupted by impacts and the fragments escaped from the parent-bodies.

Shock features recorded in ordinary chondrites have been investigated to clarify the disruption histories. Most works have focused on petrologic type 5 and 6 ordinary chondrites derived from the inner portions of the parent-bodies (e.g., Chen et al., 1996; Ohtani et al., 2004). In contrast, few works have worked on shock features recorded in petrologic type 3 and 4 ordinary chondrites derived from the outer portions of the parent-bodies (Ruzicka et al., 2015a–b), because, in general, the shock features in petrologic type 3 and 4 ordinary chondrites are not distinct compared to those in petrologic type 5 and 6 ordinary chondrites.

Miyahara et al. (2021) conduct systematic investigations of shock-induced melts and high-pressure polymorphs in ordinary chondrites and report that some petrologic type 3 ordinary chondrites have shock-induced melts and high-pressure polymorphs. Also, some petrologic type 3 ordinary chondrites with shock-induced melts include flattened chondrules. Foliation in chondrites is formed during the sedimentation of chondrules on the parent-bodies (Dodd, 1965; Martin & Mills, 1980). The foliation in chondrites also can be formed by impacts because when a shock wave propagates in a rock, uniaxial compaction occurs (Sneyd et al., 1998; Gattacceca et al., 2005).

We raise the possibility that the flattened chondrules in type 3 ordinary chondrites are due to shock metamorphism and the aspect ratios of chondrules depend on shock pressure. Several shock recovery experiments using equilibrated ordinary chondrites were conducted to clarify the shock features (e.g., Stöffler et al., 1991; Kohout et al., 2020). In contrast, shock recovery experiments using unequilibrated ordinary chondrites have not been conducted so far.

The average size of chondrules in H3 chondrites is distinct from those of L/LL3 chondrites: the mean diameters of chondrules in H3 and L/LL3 are about 450 and 500–550 μm, respectively (Friedrich et al., 2015). The flattening degree of chondrules may depend on the size distribution of chondrules. Hence, we conduct shock recovery experiments using H3 and L3 chondrites to i) reproduce shock-induced melt and chondrule flattening and ii) clarify the relationship between flattening degree and shock pressure. This study also uses several Antarctic and non-Antarctica petrologic type 3 ordinary chondrites with or without a

shock-induced melt to verify the shock recovery experiments.

2. Materials and experimental methods

2.1 Materials

Shock experiments used two petrologic-type 3 ordinary chondrites: the Allan Hills (ALH)-78084 H3 and Yamato (Y)-793375 L3. Sliced ALH-78084 H3 (Area: about 20 x 40 mm^2, thickness: about 2.73 mm) and Y-793375 L3 (Area: about 22 x 38 mm^2, thickness: about 2.08 mm) samples were allocated from the National Institute of Polar Research (NIPR), Japan. These two chondrites show a well-preserved chondritic texture suitable as starting materials for the shock experiments. Fifteen H3, twenty-three L3, and twenty-three LL3 ordinary chondrites were selected for the comparisons and verifications of the shock recovery experiments. The classification of individual samples (chemical group and petrologic type) followed the Meteoritical Society Bulletin database.

2.2 Shock experiments

The allocated ALH-78084 H3 and Y-793375 L3 chondrite samples were adhered to glasses using Crystalbond^{TM} 509. Doubly polished samples with a thickness of 1.5 mm were made by a surface grinding machine. Disc samples (φ = 6 or 12 mm) were cored out from the doubly polished samples by an ultrasonic machine. The cored-out disc samples were put in acetone for thirty hours to remove Crystalbond^{TM} and dried at 373 K for thirty hours. The prepared disc samples were kept in a closed plastic bag with a silica gel until shock experiments.

The densities of individual disc samples were calculated by measuring their thicknesses, diameters, and weights (Table 1). The disc samples were put into stainless (SUS 304) containers (30 mm diameter x 30 mm long). The disc samples were placed at a depth of 3 mm from the impact surface of the stainless container. Shock experiments used a 30-mm bore propellant gun installed at the National Institute for Materials Science (NIMS), Tsukuba, Japan. 2-mm thick steel (SUS 304) or tungsten (W) flyer plate, attached to the head of a projectile, impacted the stainless containers. Velocity just before the impact was measured with a magneto flyer method (Kondo et al., 1977). The peak shock pressure was calculated by the impedance match method assuming the sample pressure reached equilibrium with the container pressure because the experimental procedures are similar to those described by Yamaguchi & Sekine (2000). Table 1 shows the details of individual experimental conditions.

2.3 Sample analysis

Stainless containers were recovered after individual shock experiments and were

sliced open with a diamond saw and lathe to observe the cross-sections of disc samples. 1-3 slices were made from each recovered stainless container. The slices were embedded into an epoxy resin and were polished with an abrasive paper under the dry condition to reduce the exfoliation of the disc samples.

We took back-scattered electron (BSE) images of polished cross-sections by a field-emission scanning electron microscope (FE-SEM): JEOL JSM-7100F (installed at NIPR) at an accelerating voltage of 15 kV. A dedicated image processing application the Oxford AZtec installed in JEOL JSM-7100F combined all individual BSE images into one BSE image depicting the whole area of the cross-section. Subsequently, individual melts and deformation textures in the cross-sections were observed under higher magnification BSE image mode. The short and long axes of chondrules in the cross-sections were measured using the combined BSE images and dedicated image processing application SmartGrain (Tanabata et al., 2012). The measured axis lengths are apparent. The measured axis lengths (2D) were converted to the actual lengths (3D) by multiplying a factor of 1.273 (Kong et al., 2005). The angles of the long axes to an arbitrary axis were measured by the image processing application ImageJ. The total lengths of open cracks in individual cross-sections were also measured by ImageJ.

The whole area BSE images of selected petrologic type 3 ordinary chondrites were also observed by FE-SEM to measure the short and long axes of chondrules and the angles of the long axes to an arbitrary axis. Individual melts and deformation textures were observed under higher magnification BSE image mode. The measurement procedures of the chondrules are as same as the samples recovered after shock experiments. The mineralogy of melts was determined using a laser micro-Raman spectrometer: Renishaw inVia (at NIPR). An optical microscope was used to focus the excitation laser beam (the 532 nm line of green laser). The laser power was kept at < ~7 mW to reduce laser beam damage. The acquisition time was 10–60 s. For each phase, the Raman spectrum was acquired in the spectral region of 200 to 1500 cm^{-1}.

3. Results

3.1 Petrologic descriptions of starting materials

Figures S1–2 show the petrologic thin sections of unshocked ALH-78084 H3 and Y-793375 L3 chondrites. No distinct shock features such as undulatory extinction and fractures were observed in the petrologic thin sections. Figures S3a–b show the representative petrological textures of ALH-78084 H3 and Y-793375 L3 chondrites,

respectively. Melts were not found in ALH-78084 H3 and Y-793375 L3 chondrites. A small amount of weathering vein occurred in ALH-78084 H3 chondrite (Fig. S3a).

The long and short axes of chondrules in ALH-78084 H3 and Y-793375 L3 chondrites were measured using the petrologic thin sections. The distributions of long and short axes did not follow the Gaussian distribution (Figs. S4a–d). The long and short axes of chondrules in ALH-78084 H3 chondrite were respectively 429 μm and 352 μm (median, n = 258) (Table 2). Those in Y-793375 L3 chondrite were 773 μm and 634 μm (n = 143) (Table 2). The aspect ratios of chondrules in ALH-78084 H3 and Y-793375 L3 chondrites were respectively 1.19 and 1.22 (median) (Figs. S4e–f, Table 2). The number densities of chondrules in ALH-78084 H3 and Y-793375 L3 chondrites were 2.12 and 1.18 mm^{-2}.

3.2 Experimentally shocked ALH-78084 H3 chondrite

Shock experiments were conducted in the shock pressure range from 11 to 43 GPa (Table 1). Six samples were successfully recovered after shock experiments. Three polished slices were prepared from each recovered sample except for Shot No. H_7. Figure S5 shows the whole area BSE images depicting the cross-sections of recovered samples. Some recovered samples were concave in the shapes. With increasing shock pressure, the degree of concave became bigger (Fig. S5). A part of sample Shot No. H_6 (42.9 GPa) came out into the stainless container (Fig. S5e). Open cracks cutting chondrules occurred in most samples and arranged sub-parallel to shockwave front (Figs. 1a, S5). Figure 2a shows the drawing of open cracks in each shot. The length of open cracks per unit square in each shot is shown in Table 2.

Some olivine grains in shocked samples had irregular and/or planar fractures (Fig. 1b). Melts were found from all the shocked samples. Melts occurred along boundaries between chondrules and matrices consisting of fine-grained materials (Fig. 1c). In most cases, each melt was isolated and not interconnected with each other. The melts consisted of quenched melts and mineral and/or chondrule fragments. The quenched melts consisted of fine-grained silicate minerals (olivine and pyroxene), glasses, and metals (Fig. 1d). The mineral and chondrule fragments entrained in the melts were rounded due to melting (Fig. 1d). The metals, which were in the shapes of amoeba or spherule, consisted of metallic Fe-Ni or metallic Fe-Ni–iron-sulfide with a eutectic texture (Figs. 1d–f). Voids occurred in the melts (Figs. 1e–f). No high-pressure polymorphs were found from the quenched melts or mineral and/or chondrule fragments.

The long and short axes of chondrules and chondritic fragments in the shocked samples were measured. The aspect ratios are shown in Table 2 and Figure 3a. The number of measurable chondrules decreased with increasing shock pressure

because the deformation degree of sample containers increased (Fig. S5). All the aspect ratios of chondrules in the shocked samples (1.19–1.57) were bigger than that of starting material (1.19)(Table 2). Azimuths of long axes to an impact surface were measured (Table S1, Fig. S6). Chondrules in Shot No. H_7 were not measured because its cross-section was too small for measurements. Only textural observations by FE-SEM were conducted for Shot No. H_7.

3.3 Shocked Y-793375 L3 chondrite

Shock experiments were conducted in the shock pressure range from 11 to 43 GPa for Y-793375 L3 (Table 1). Six samples were successfully recovered after shock experiments. Three polished slices were prepared from each recovered sample. Figure S7 shows the whole area BSE images depicting the cross-sections of recovered samples. Some recovered samples were concave in the shapes and the degree became bigger with increasing shock pressure (Figs. 2b, S7). A part of sample Shot No. L_6 (42.5 GPa) came out into the stainless container (Fig. S7f). Open cracks arranging sub-parallel to shockwave occurred in the shocked samples (Fig. 4a). Figure 2b shows the drawings of open cracks in each shot. The length of open cracks per unit square in each shot is shown in Table 2.

Some olivine grains in shocked samples had irregular and/or planar fractures (Fig. 4b). Melts were found from all the shocked samples. Isolated melting occurred along with boundaries between chondrules and matrices (Fig. 4c). The textures and constituents of melts were similar to those of ALH-78084 H3 chondrite (Figs. 4c–f). Some melted chondrule glasses had a flow-like texture (Fig. 4e). One-third of the cross-section of Shot No. L_4 (26.4 GPa) was melted (Figs. S7d, S8a). The quenched melts consisted mainly of fine-grained pyroxene with a dendrite texture, glasses, and metallic Fe-Ni–FeS with a eutectic texture (Figs. S8b–c). Voids occurred in the glasses and also in some metals (Fig. S8c). No high-pressure polymorphs were found from all the shocked samples.

The long and short axes of chondrules (and chondritic fragments) and the aspect ratios in the shocked samples are shown in Table 2. All the aspect ratios of shocked samples (1.36–1.75) were bigger than that of starting material (1.22)(Table 2). The azimuths of long axes to an impact surface are shown in Table S1 and Figure S9.

3.4 Petrologic type 3 ordinary chondrites

Shock-induced melts and aspect ratios of chondrules (and chondritic fragments) in selected H/L/LL3 ordinary chondrites were investigated. Typical whole area BSE images of investigated H/L/LL3 ordinary chondrites are shown in Figure S10. The modes of melting are shown in Tables S2–4 and the definition of

melting followed Miyahara et al. (2021): i) pocket, ii) line, and iii) network. The textures and constituents of shock-induced melts were similar to those of shocked ALH-78084 H3 and Y-793375 L3 chondrites (Figs. 5a–b). Melting occurred also in some fragments of chondrule glasses in contact with the shock-induced melts (Figs. 5c–d). Void, which was ubiquitously observed in shocked ALH-78084 H3 and Y-793375 L3 chondrites, did not occur in the shock-induced melts of H/L/LL3 ordinary chondrites. Distinct open cracks cutting chondrules, which was observed in shocked ALH-78084 H3 and Y-793375 L3 chondrites, were not observed in H/L/LL3 ordinary chondrites. By contrast, open cracks occurred in the shock-induced melts of some L/LL3 ordinary chondrites (Fig. 5e).

The long and short axes of chondrules (and chondritic fragments) in H/L/LL3 chondrites are shown in Tables S2–4. In fifteen H3 chondrites, only Y-981139 H3 chondrite included a shock-induced melt (Table S2). No high-pressure polymorphs occurred in Y-981139 H3 chondrite. The difference in the aspect ratios between H3 ordinary chondrites without (1.17–1.28) or with shock-induced melts (1.24) was not clear (Fig. 6, Table S2). In twenty-three L3 chondrites, sixteen L3 chondrites included shock-induced melts (Table S3). Y-981327 chondrite had a pervasive shock-induced melt (Figs. S10b–c). Asuka (A)-880870, A-881096, Y-86706, and Northwest Africa (NWA) 8664 L3 chondrites included Na-pyroxene and coesite as high-pressure polymorphs (Figs. 5e–f, Table S3). The aspect ratios of chondrules in L3 ordinary chondrites without or with shock-induced melts were 1.20–1.36 and 1.27–1.75, (Table S3). The aspect ratio of chondrules in Y-981327 chondrite was higher (1.75) than others (Table S3, Fig. 7). In twenty-three LL3 ordinary chondrites, five LL3 ordinary chondrites included shock-induced melts (Table S4, Fig. 8). A-881199 and A-881981 LL3 chondrites included Na-pyroxene and coesite as high-pressure polymorphs. The aspect ratios of chondrules in LL3 ordinary chondrites without or with shock-induced melts were 1.16–1.41 and 1.31–1.54 (Table S4). The angles of long axes to arbitrary axes in H/L/LL3 ordinary chondrites were also measured (Tables S2–4).

4. Discussion

4.1 shock-induced melting

Melting occurs in all the shocked ALH-78084 H3 and Y-793375 L3 chondrite samples and the melts have evidence of immiscibility between silicate melts and metallic melts under high-pressure (e.g., Kato & Ringwood, 1989). The melts in the shocked samples consist of fine-grained silicate minerals (olivine and/or pyroxene), glasses, and the spherules of metallic Fe-Ni or metallic Fe-Ni–

iron-sulfide with a eutectic texture (Figs. 1c–f, 4c–d). Some spherules of fine-grained silicate mineral assemblages are included in the spherules of metallic Fe-Ni or metallic Fe-Ni–iron-sulfide with a eutectic texture (Figs. 1c–d, 4f). All these features indicate that melting occurs under high-pressure.

The temperature in the shocked ALH-78084 H3 and Y-793375 L3 chondrite samples during the impact is not homogeneous. Most chondrules in shocked samples do not show clear evidence of melting (Figs. S5, S7). Melting occurs in matrices in contact with chondrules (Figs. 1c, 4c). The porosity of matrices is higher compared to that of chondrules because the matrices are fine-grained crystal assemblages. When compression wave propagates in un-equilibrated chondrites, their matrices with relatively low shock impedance decrease their volumes more drastically than their chondrules with relatively high shock impedance. The large volume decrease induces a temperature spike resulting in local melting in the matrices.

The petrologic structure of un-equilibrated chondrites, which consists of coarse-grained chondrules and fine-grained materials (matrices), makes shock-induced melting easier under low pressure. Hirata et al. (2009) conducted shock experiments using mimic porous primitive chondritic materials (initial porosity: 35±5%). Shock veins occur above 25 GPa in the shocked mimic porous primitive chondritic materials. By contrast, shock-induced melting occurs in the un-equilibrated H3 and L3 ordinary chondrites with low porosities even at 11 GPa. A local temperature spike under low shock pressure in un-equilibrated chondrites is predicted by numerical simulation (Bland et al., 2014). The petrologic structure of a target becomes a more important factor in some cases than its porosity for shock-induced melting.

If petrologic type 3 ordinary chondrites expose on asteroids, the surfaces have experienced melting along with brecciation. The onion shell model proposes that petrologic type 3 ordinary chondrites have made up the outmost layers of ordinary chondrite parent-bodies (e.g., Trieloff et al., 2003). Shock experiments prove that even if the impact of 0.57 km/sec causes shock-induced melting in petrologic type 3 ordinary chondrites. Following the Rankine-Hugoniot equation, shock pressure depends on impact velocity. In general, the existence of shock-induced melts in ordinary chondrites implies high shock pressure. However, petrologic type 3 ordinary chondrites do not apply the criterion. The impact velocity of 0.57 km/sec is much lower compared to the most probable impact velocity in the asteroid belt (4.4 km/sec) (Bottke et al., 1994). The surfaces of S-type asteroids may like lunar regolith that includes brecciated rocks and melts.

Heating by shock-induced melts does not significantly affect thermal metamorphism in petrologic type 3 ordinary chondrites. Numerical simulations indicate that the temperature of matrices during the impact becomes higher with increasing chondrule/matrix ratios at the same impact speed in unequilibrated chondrites (Bland et al., 2014). The maximum temperature in petrologic type 3 ordinary chondrites is higher compared to carbonaceous chondrites because the former includes a few amounts of matrices (Weisberg et al., 2006). The shock-induced melts in the matrices may work as a heat source for thermal metamorphism. However, the heat sources in the petrologic type 3 ordinary chondrites are small due to the limited amounts of matrices. Hence, the shock-induced melts do not affect the bulk-rock temperature of petrologic type 3 ordinary chondrites.

Voids occur in the shock-induced melts of shocked ALH-78084 H3 and Y-793375 L3 chondrite samples (Figs. 1f, 4f), which is due to the degassing of volatile elements during the decompression stage. Parts of shocked chondrites melt, and volatile elements are dissolved into the melts under high-pressure. The degassing occurs before the melts are quenched. Decompression is initiated when a rarefaction wave catches up the compression wave. Assuming that the longitudinal wave velocities of chondrite and stainless container at ambient pressure conditions are 6 and 5.77 km/sec., respectively, the propagations of compression and rarefaction waves in the sample containers are calculated. The rarefaction wave achieves the backside of samples in 1–2 μ sec after the impact. The quenching of melts is initiated by thermal conduction into the stainless container. The degassing is due to the limited duration of high-pressure compared to the time required for the quenching.

Shock-induced melts in investigated H/L/LL3 chondrites do not include voids (Fig. 5), which is due to the difference in the durations of high-pressure between shock experiments and natural impact events. The duration of high-pressure recorded in several ordinary chondrites is estimated using the kinetics of high-pressure polymorphs or diffusion rates of trace elements (Ohtani et al., 2004; Beck et al., 2005; Xie et al., 2006). The durations (several milliseconds to seconds) are much longer than the shock experiments (several microseconds). Hence, the melts can be quenched under high-pressure.

Some quenched melts include fractures (Figs. 5e–f), which is due to a heterogeneous compression in un-equilibrated chondrites. The quenched melts, which are quenched under high-pressure after melting, is denser than original matrices. Chondrules are less compacted due to low porosity during the compression

stage. The fractures in the melts are induced by the tensile failure of the quenched melts during the decompression stage.

4.2 Shock-induced flattening of chondrules

The aspect ratios of chondrules in shocked ALH-78084 H3 and Y-793375 L3 chondrites increase with increasing shock pressure (Fig. 3c), indicating that the chondrules are deformed by shock metamorphism. Shock recovery experiments prove that both the chondrule flattening along with melting occur in type 3 ordinary chondrites by shock metamorphism. Liner fitting is conducted for plotted data by the least-squares method (Fig. 3c). The aspect ratios at ambient pressure are fixed with the aspect ratios of chondrules in starting materials. The calculated slopes for ALH-78084 H3 and Y-793375 L3 chondrites are 0.88×10^{-2} and 1.09×10^{-2}. The aspect ratios of chondrules in experimentally shocked Murchison CM2 and Allende CV3 chondrites (Tomeoka et al., 1999; Nakamura et al., 2000) are also plotted in Figure 3c. The calculated slopes for Murchison CM2 and Allende CV3 chondrites are 1.40×10^{-2} and 2.38×10^{-2}.

Considering the interquartile range, the flattening degree of chondrules in Y-793375 L3 chondrite is a bit higher than that in ALH-78084 H3 chondrite (Figs. 3a–c), which is due to the grain refining of chondrules. There are no distinct differences in the densities and chondrule/matrix ratios between ALH-78084 H3 and Y-793375 L3 chondrites as starting materials (Table 1). By contrast, the size of chondrules in ALH-78084 H3 chondrite is finer than that of Y-793375 L3 chondrites (Table 1). A petrologic-type 3 ordinary chondrite is an assemblage of chondrules, which can be regarded as a polycrystal. Yield stress (σ_y) can be described by the Hall-Petch relationship,

$$\sigma_y = \sigma_0 + k_y d^{-1/2}$$

where σ_0, k, and d are the internal stress, the strengthening coefficient, and grain size, respectively. Following the Hall-Petch relationship, the yield stress of petrologic type 3 ordinary chondrites increases with decreasing the size of chondrules. The strengthening by grain refinement inhibits the flattening of chondrules in ALH-78084 H3 chondrite.

The size sorting of chondrules also affects the flattening degree of chondrules. The size of chondrules in ALH-78084 H3 chondrite is sorted, whereas that in Y-793375 L3 chondrite is scattered (Fig. S4). In petrologic type 3 ordinary chondrites consisting of chondrules with varied sizes, the yield stress is heterogeneous. The heterogeneous yield stress decreases the strength of Y-793375 L3 chondrite as a bulk-rock, which increases the flattening degree of chondrules.

The relative abundance of matrices (+ lithic or mineral fragments) does not significantly affect the flattening degree of chondrules. The relative abundances of chondrules and matrices (+ lithic or mineral fragments) in Allende CV3 chondrites are 35–43 % and 41– 55 % (McSween, 1977; Ebel et al., 2016). Those in Murchison CM2 are ~16 % and ~75 % (McSween, 1979). The relative abundances of chondrules in ALH-78084 H3 (chondrule: 65 %, matrix: 15 %) and Y-793375 L3 (chondrule: 63 %, matrix: 23 %) chondrites are much higher than Murchison CM2 and Allende CV3 chondrites. However, the flattening degree of chondrules in Murchison CM2 chondrite is similar to those of ALH-78084 H3 and Y-793375 L3 chondrites.

A bulk-rock porosity does not also affect the flattening degree of chondrules. The porosities of Allende CV3 and Murchison CM2 are 16.9–27.9 % and 18.8–24.9 % (Macke et al., 2011). Although the porosities of ALH-78084 H3 and Y-793375 L3 chondrites are not measured, the average porosities of H and L ordinary chondrites are 7.0 and 5.6 % (Consolmagno et al., 2008). However, there are no distinct differences in the flattening degrees between H/L3 ordinary chondrites and Murchison CM2 chondrite. The flattening degree of chondrules in Allende CV3 chondrite is much higher than Murchison CM2 chondrite although there are no distinct differences in their physical properties (Fig. 3c). We could not find an adequate factor to explain the difference.

Long axes of flattened chondrules have a weak preferred orientation because of uniaxial compression during shock metamorphism. The long axes of chondrules in ALH-78084 H3 and Y-793375 L3 chondrites do not arrange homogeneously (Figs. S6, S9). We first draw the Lorenz curves using the azimuths of long axes in starting materials and each shocked sample (Table S1, Figs. S11a–b) and calculate the Gini coefficients to evaluate the preferred orientation (Table 2). The Gini coefficients of long axes in ALH-78084 H3 and Y-793375 L3 chondrites as starting materials are 0.33 and 0.32, respectively (Table 2). If the long axes do not have preferred orientations, the Gini coefficient becomes null. Although the Gini coefficients of ALH-78084 H3 and Y-793375 L3 chondrites keep small, the values become bigger slightly with increasing shock pressure (Fig. S11c).

Open cracks in shocked samples are induced by tensile failure when compressive stress is reflected at the free surface of a stainless container and becomes tensile stress. The lengths of open cracks in shocked ALH-78084 H3 and Y-793375 L3 chondrites increase with increasing shock pressure (Fig. 3d). However, the linear relationship between shock pressure and lengths is not clear. It is difficult to adopt the relationship for the estimation of shock pressure.

4.3 Estimation of shock pressure by aspect ratios of chondrules

The shock pressure recorded in each H/L/LL3 ordinary chondrite is estimated using by adopting the aspect ratios of chondrules (median) into the empirical formulae obtained from shock experiments to estimate shock pressure (Tables S2–4). The empirical formulae obtained from ALH-78084 H3 and Y-793375 L3 chondrites are adopted for H3 and L/LL3 ordinary chondrites, respectively. Figures 6–8 show box plots showing the aspect ratios of chondrules in each H/L/LL3 ordinary chondrite and estimated shock pressure. The ordinary chondrites in each figure are sorted according to the aspect ratios.

No difference is found in estimated shock pressure between H3 ordinary chondrites with a shock-induced melt (Gray-colored box) or without a shock-induced melt (White-colored melt) (Fig. 6). The estimated shock pressure of Y-981139 H3 chondrite with a shock-induced melt is 4.8 GPa (Table S2). The estimated shock pressure of H3 ordinary chondrites without shock-induced melts is up to about 10 GPa. Several estimated shock pressure values are below zero, which is impossible.

By contrast, the estimated shock pressure of L/LL3 ordinary chondrites with shock-induced melts is higher than those of L/LL3 ordinary chondrites without shock-induced melts (Tables S3–4, Figs. 7–8). The estimated shock pressure of L3 ordinary chondrites without shock-induced melts is less than 7.8 GPa except for A-881244 L3 chondrite. The estimated shock pressure of most L3 ordinary chondrites with shock-induced melts is higher than 7.8 GPa. The chondrules of Y-981327 L3 chondrite have a very high aspect ratio (1.75) and the estimated shock pressure is also very high (48.2 GPa)(Table S3). Y-981327 L3 chondrite is heavily shocked because it has the extensive shock-induced melts (Figs. S10b–c).

No obvious correlation is found between estimated shock pressure and high-pressure polymorphs (Tables S3–4). No wonder that there is no correlation among shock pressure estimated from the aspect ratios of chondrules, shock-induced melts, and high-pressure polymorphs. The formations of high-pressure polymorphs are controlled by kinetics. Even if both high-pressure and -temperature conditions required for the formation of high-pressure polymorphs are achieved, high-pressure polymorphs cannot form if their duration is not enough. It is also possible that high-pressure polymorphs, which formed during compression and equilibrium stages once, back-transforms into their low-pressure polymorphs during the subsequent adiabatic decompression stage if the cooling is slow.

Some estimated shock pressure values are invalid, which is due to the deviation of aspect ratios of intact chondrules that are free from shock metamorphism. The mean aspect ratio of intact chondrules in LL3 chondrites is 1.2 ±

0.18 (n = 719) (Nelson & Rubin, 2002), which coincides with the aspect ratios of chondrules (and chondritic fragments) in ALH-78084 H3 and Y-793375 L3 chondrites as starting materials (Table 2). Considering the standard deviation, in the case of less shocked ordinary chondrites, some shock pressure values estimated from the aspect ratios of chondrules becomes invalid. In contrast, some estimated shock pressure values become overestimated.

The preferred orientations of long axes of chondrules become distinct in highly shocked L/LL3 chondrites, especially including shock-induced melts (Tables S2–4, Fig. S12). The Gini coefficients increase with increasing shock pressure in L/LL3 chondrites. The L/LL3 chondrites including shock-induced melts have higher Gini coefficients than those without melts. The degrees of preferred orientations in L/LL3 chondrites are higher compared to those of experimentally shocked chondrites. The variance is due to the differences in the duration of compression between shock experiments and natural impacts although all impacts in nature do not have long compression time.

To conclude, it is difficult to use the aspect ratios of chondrules for the quantitative estimation of shock pressure in petrologic type 3 ordinary chondrites. Repeated low-velocity impacts may increase the aspect ratios of chondrules gradually, which is proved by the shock experiments of Allende CV3 chondrite (Nakamura et al., 2000). The aspect ratios of chondrules in pre-heated Allende CV3 chondrite become bigger than those of chondrules at room temperature. Ordinary chondrite parent-bodies had a heart source such as ^{26}Al when they were born. If impacts occur on hot parent-bodies, the flattening degree of chondrules becomes bigger than that of chondrules on cold parent-bodies. Although chondrules with a high aspect ratio and preferred orientation become a screening standard for strong shock metamorphism, it does not work as a quantitative shock pressure barometer.

5. Conclusions

1) Shock experiments using ALH-78084 H3 and Y-793375 L3 chondrites prove that shock-induced melting occurs in petrologic type 3 chondrites beyond 11 GPa at least. The melting occurs at boundaries between chondrules and matrices.
2) Shock-induced flattening of chondrules occurs in petrologic type 3 chondrites. The flattening degree increases with increasing shock pressure.
3) There is no significant difference in the flattening degree of chondrules between carbonaceous and ordinary chondrites. The flattening degree does not depend significantly on the densities, porosities, and chondrule/matrix ratios of chondrites. Finally, by considering the relationships between the aspect ratios of

chondrules and shock pressure in carbonaceous and ordinary chondrites, the aspect ratios in unequilibrated chondrites (R_{cho}) can be expressed following the linear equation: R_{cho} = 0.011 (±1) × Pressure (GPa) + 1.18 (±3).

4) The long axes of chondrules have a preferred orientation and the degree increases with increasing shock pressure.
5) Natural L/LL3 ordinary chondrites with shock-induced melts have higher aspect ratios and preferred orientations of chondrules than those without shock-induced melts.
6) It is difficult to determine quantitatively shock pressure in petrologic type 3 chondrites using the empirical formula between the aspect ratios of chondrules and shock pressure.

Acknowledgments

This study was supported by Grants-in-Aid for Scientific Research, no. 18H01269 from the Ministry of Education, Culture Sports, Science, and Technology (MEXT) to M.M. This study was also financially supported by NIPR through General Collaboration Projects nos. 26-31 and KP-307. We acknowledge Dr. M. Kayama for providing the design drawing of a sample container used in this shock experiment. The measured aspect ratios and azimuth of chondrules are available in Miyahara (2021).

References

Beck P., Gillet Ph., El Goresy A., & Mostefaoui S. (2005). Timescales of shock processes in chondritic and martian meteorites. *Nature* 435, 1071–1074.

Bland P.A., Collins G.S., Davison T.M., Abreu N.M., Ciesla F.J., Muxworthy A.R., & Moore J. (2014). Pressure–temperature evolution of primordial solar system solids during impact-induced compaction. *Nature Communications* 5, 5451 doi: 10.1038/ncomms6451.

Bottke Jr. W.F., Nolan M.C., Greenberg R., & Kolvoord R.A. (1994). Velocity distributions among colliding asteroids. *Icarus* 107, 255–268.

Chen M., Sharp T.G., El Goresy A., Wopenka B., & Xie X. (1996). The majorite-pyrope + magnesiowüstite assemblage: Constraints on the history of shock veins in chondrites. *Science* 271, 1570–1573.

Consolmagno G.J., Brittb D.T., & Macke R.J. (2008). The significance of meteorite density and porosity. *Chemie der Erde* 68, 1–29.

Dodd Jr. R.T. (1965). Preferred orientation of chondrules in chondrites. *Icarus* 4, 308–316.

552 Ebel D.S., Brunner C., Konrad K., Leftwich K., Erb I., Lu M., Rodriguez H., Ellen J.
553 Crapster-Pregont E.J., Friedrich J.M., & Weisberg M.K. (2016). Abundance,
554 major element composition and size of components and matrix in CV, CO and
555 Acfer 094 chondrites. *Geochimica et Cosmochimica Acta* 172, 322–356.
556 Friedrich J.M., Weisberg M.K., Ebel D.S., Biltz A.E., Corbett B.M., Iotzov I.V.,
557 Khan W.S., & Wolman M.D. (2015). Chondrule size and related physical
558 properties: A compilation and evaluation of current data across all meteorite
559 groups. *Chemie der Erde* 75, 419–443.
560 Gattaccecaa J., Rochette P., Denise M., Consolmagno G., & Folco L. (2005). An
561 impact origin for the foliation of chondrites. *Earth and Planetary Science Letters*
562 234, 351–368.
563 Hirata N., Kurita K., & Sekine T. (2009). Simulation experiments for shocked
564 primitive materials in the Solar System. *Physics of the Earth and Planetary*
565 *Interiors* 174, 227–241.
566 Kato T. & Ringwood A.E. (1989). Melting relationships in the system Fe-FeO at high
567 pressures: Implications for the composition and formation of the earth's core.
568 *Physics and Chemistory of Minerals* 16, 524–538.
569 Kondo K.I., Sawaoka A., & Saito S. (1977). Magneto flyer method for measuring
570 gas-gun projectile velocities. *Review of Scientific Instruments* 48, 1581–1582.
571 Kong M., Bhattacharya R.N., James C., & Basu A. (2005). A statistical approach to
572 estimate the 3D size distribution of spheres from 2D size distributions. *Geological*
573 *Society of America Bulletin* 117, 244–249.
574 Kohout T., Petrova E.V., Yakovlev G.A., Grokhovsky V.I., Penttilä A., Maturilli A.,
575 Moreau J.G., Berzin S.V., Wasiljeff J., Danilenko I.A., Zamyatin D.A.,
576 Muftakhetdinova R.F., & Heikkilä M. (2020). Experimental constraints on the
577 ordinary chondrite shock darkening caused by asteroid collisions. Astronomy &
578 Astrophysics, doi: https://doi.org/10.1051/0004-6361/202037593.
579 Martin P.M. & Mills A.A. (1980). Preferred chondrule orientations in meteorites.
580 *Earth and Planetaey Science Letters* 51, 18–25.
581 Macke R.J., Consolmagno G.J., & Britt D.T. (2011). Density, porosity, and magnetic
582 susceptibility of carbonaceous chondrites. *Meteoritics and Planetary Science* 46,
583 1842–1862.
584 McSween Jr. H.Y. (1977). Petrographic variations among the carbonaceous
585 chondrites of the Vigarano type. *Geochimica et Cosmochimica Acta* 41, 1777–
586 1790.
587 McSween Jr. H.Y. (1979). Alteration in CM carbonaceous chondrites inferred from
588 modal and chemical variations in matrix. *Geochimica et Cosmochimica Acta* 43,

589 1761–1765.
590 Miyahara M., Yamaguchi A., Saitoh M., Fukimoto K., Sakai T., Ohfuji H., Tomioka
591 N., Kodama Y., & Ohtani E. (2020). Systematic investigations of high-pressure
592 polymorphs in shocked ordinary chondrites. *Meteoritics and Planetary Science*.
593 doi: 10.1111/maps.13608.
594 Miyahara M. (2021) Aspect ratios and azimuth of chondrules in ordinary chondrites.
595 doi.org/10.6084/m9.figshare.14060870
596 Nakamura T., Tomeoka K., Takaoka N., Sekine T., & Takeda H. (2000).
597 Impact-induced textural changes of CV carbonaceous chondrites: Experimental
598 reproduction. *Icarus* 146, 289–300.
599 Nelson V. & Rubin A.E. (2002). Size-frequency distributions of chondrules and
600 chondrule fragments in LL3 chondrites: Implications for parent-body
601 fragmentation of chondrules. *Meteoritics and Planetary Science* 37, 1361–1376.
602 Ohtani E., Kimura Y., Kimura M., Takata T., Kondo T., & Kubo T. (2004). Formation
603 of high-pressure minerals in shocked L6 chondrite Yamato 791384: Constraints on
604 shock conditions and parent body size. *Earth and Planetary Science Letters* 227,
605 505–515.
606 Ruzicka A.M., Hutson M., Friedrich J.M., Bland P.A., & Pugh R. (2015a). Northwest
607 Africa 8709: A rare but revealing type 3 ordinary chondrite melt breccia. *78th*
608 *Annual Meeting of the Meteoritical Society*, 5348.pdf.
609 Ruzicka A.M., Grossman J., Bouvier A., Herd C.D.K., & Agee C.B. (2015b). *The*
610 *Meteoritical Bulletin*, No. 101.
611 Sneyd D.S., McSween H.Y., Sugiura N., Strangway D.W., & Nord G.L. (1988).
612 Origin of petrofabrics and magnetic anisotropy in ordinary chondrites. *Meteoritics*
613 23, 139–149.
614 Stöffler D., Keil K., & Scott E.R.D. (1991). Shock metamorphism of ordinary
615 chondrites. *Geochimica et Cosmochimica Acta* 55, 3845–3867.
616 Tanabata T., Shibaya T., Hori K., Ebana K., & Yano M. (2012). SmartGrain:
617 High-throughput phenotyping software for measuring seed shape through image
618 analysis. *Plant Physiology* 160, 1871-1880.
619 Tomeoka K., Yamahana Y., & Sekine T. (1999). Experimental shock metamorphism
620 of the Murchison CM carbonaceous chondrite. *Geochimica et Cosmochimica Acta*
621 63, 3683–3703.
622 Trieloff M., Jessberger E.K., Herrwerth I., Hopp J., Fiéni C., Ghélis M.,
623 Bourot-Denise M., & Pellas P. (2003). Structure and thermal history of the
624 H-chondrite parent asteroid revealed by thermochronometry. *Nature* 422, 502–
625 506.

Weisberg M.K., McCoy T.J., & Krot A.N. (2006). Systematic and evolution of meteorite classification. In Meteorites and the early solar system II (e.d. by Lauretta and McSween), The university of Arizona Press, Tucson, pp19–52.

Xie Z., Sharp T. G., & DeCarli P.S. (2006). High-pressure phases in a shock-induced melt vein of the Tenham L6 chondrite: Constraints on shock pressure and duration. *Geochimica et Cosmochimica Acta* 70, 504–515.

Yamaguchi A. & Sekine T. (2000). Monomineralic mobilization of plagioclase by shock: an experimental study. *Earth and Planetary Science Letters*175, 289–296.

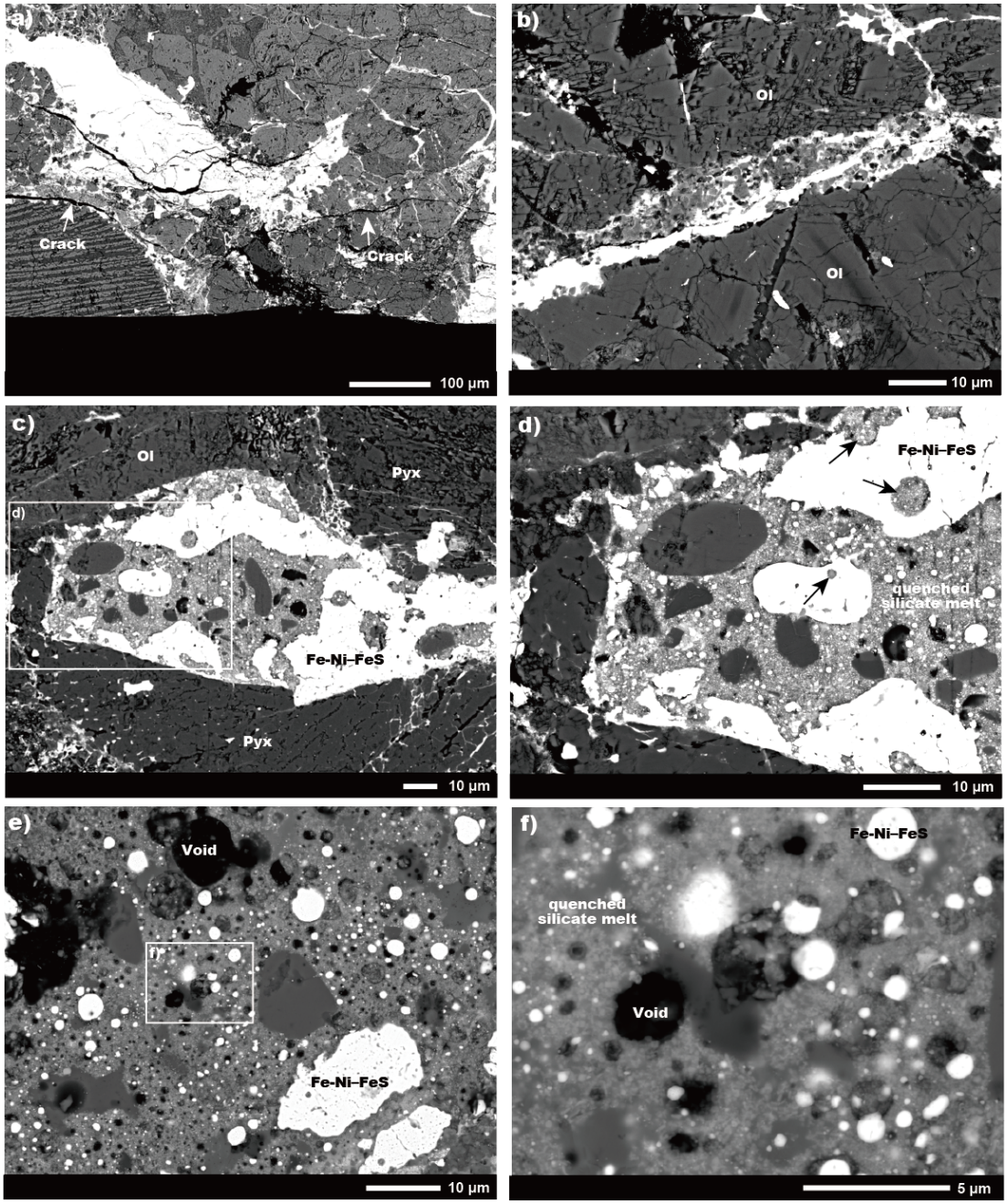

Figure 1. BSE images showing shocked ALH-78084 H3 chondrite. a) Open cracks sub-parallel to a shockwave front (H_1_3). b) Planar or irregular cracks occurred in some olivine grains (H_2_2), c) Melt between chondrules (H_3_3), d) High-magnification image of a white-colored box in c). Mineral fragments entrained into the melt were rounded. Metals include spherules of quenched silicate melt (indicated by dark-colored arrows). e) Melt consisting of quenched silicate melts, metals, mineral fragments, and voids (H_4_3), f) High-magnification image of a white-colored box in e). Ol: olivine, Pyx: pyroxene, Fe-Ni: metallic Fe-Ni, FeS: iron-sulfide.

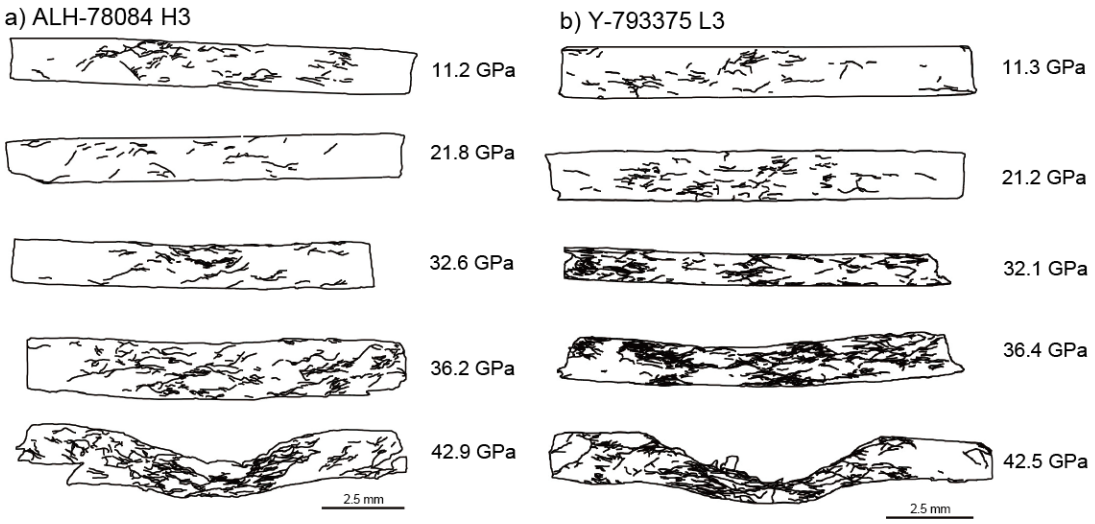

Figure 2. Representative drawings of shocked samples. a) ALH-78084 H3 and b) Y-793375 L3 chondrites. The upper direction is the impact surface.

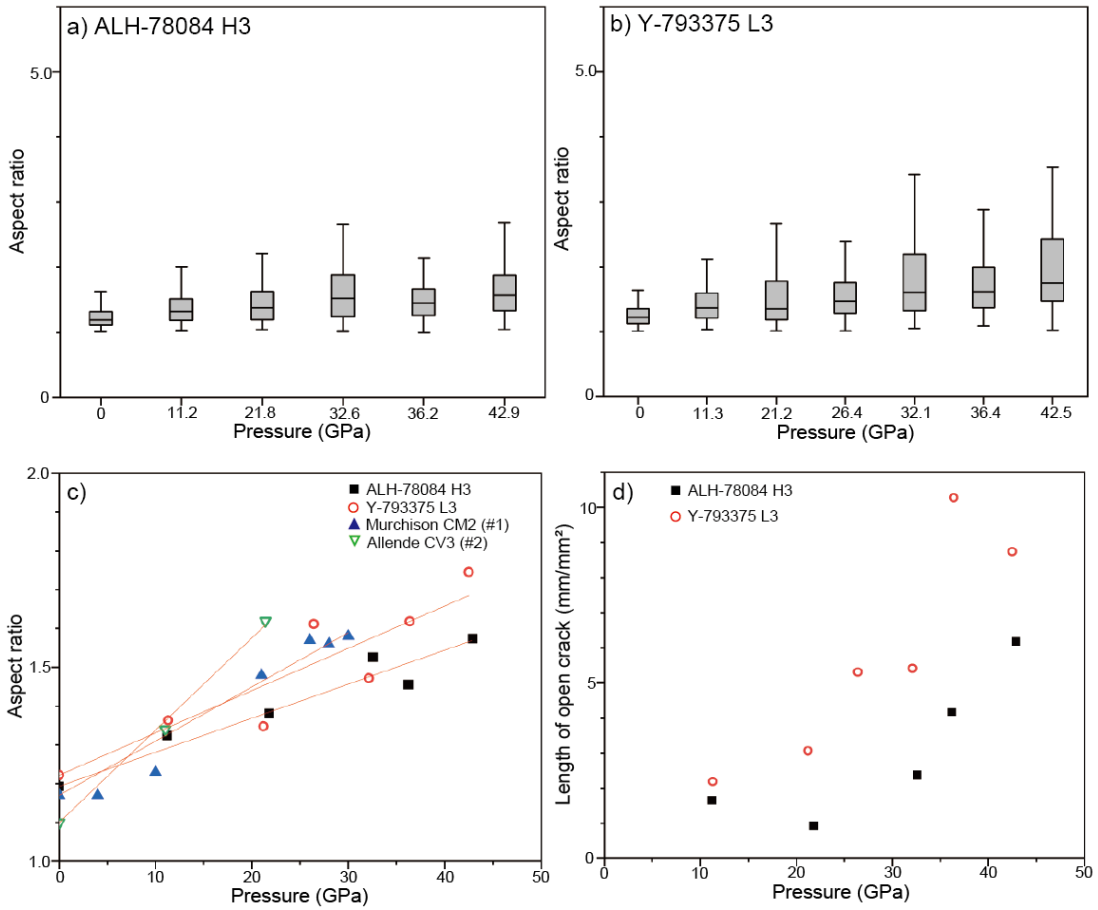

Figure 3. The morphological properties of chondrules. a) Relationship between shock pressure and the aspect ratios of chondrules. b) Relationship between shock pressure and the lengths of open cracks. #1 Tomeoka et al. (1999), #2 Nakamura et al. (2000)

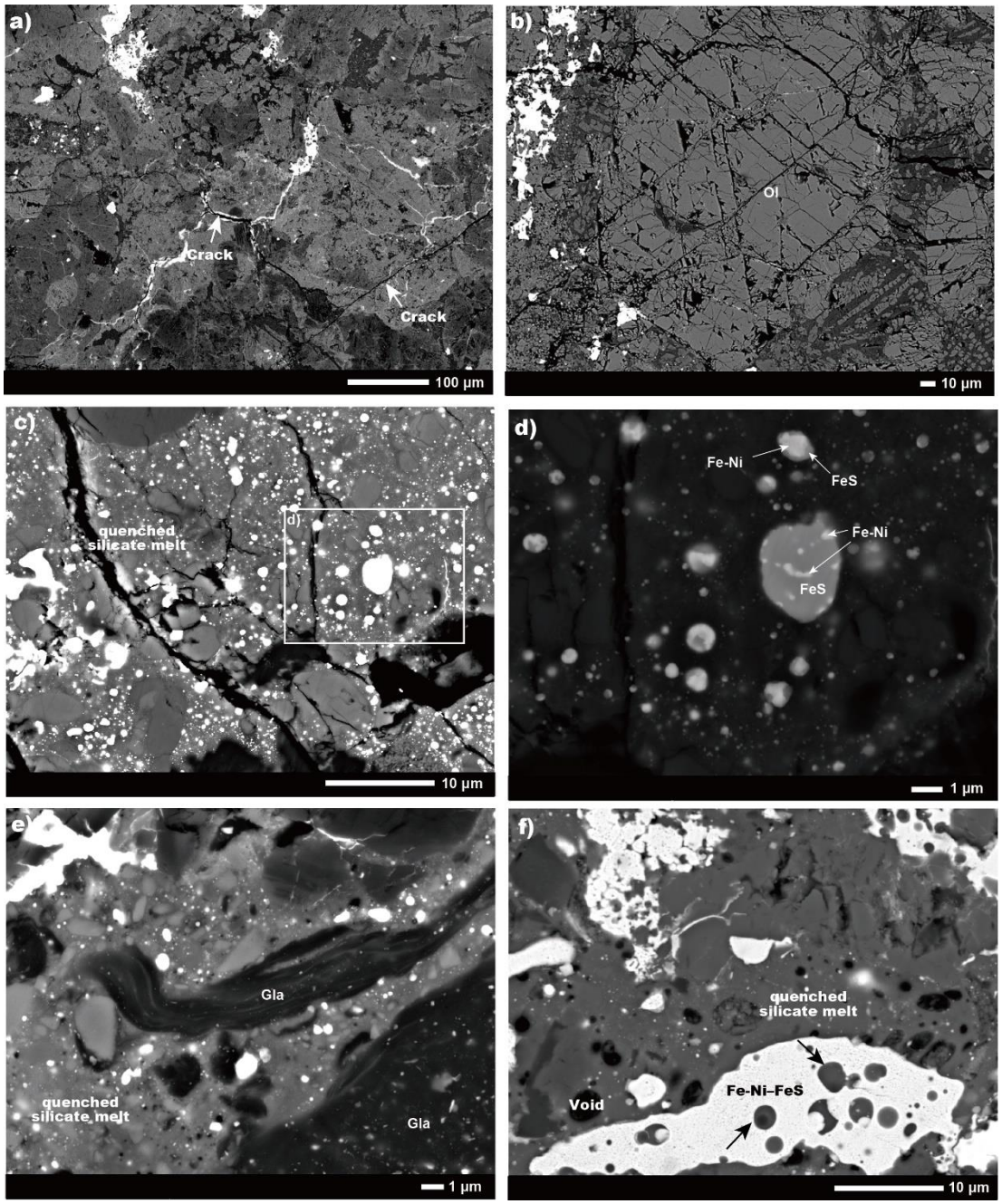

Figure 4. BSE images showing shocked Y-793375 L3 chondrite. a) Open cracks sub-parallel to a shockwave front (L_1_2), b) Planar- and irregular-fractures in some olivine grains (L_2_3), c) Melt between chondrules (L_2_3), d) High-magnification image of a white-colored box in c). The spherules of metallic Fe-Ni–FeS with a eutectic texture. e) Melted chondrule glasses in the melt (L_6_1). f) Metals including the spherules of quenched silicate melts (L_5_3). Ol: olivine, Pyx: pyroxene, Fe-Ni: metallic Fe-Ni, FeS: iron-sulfide, Gla: chondrule glass.

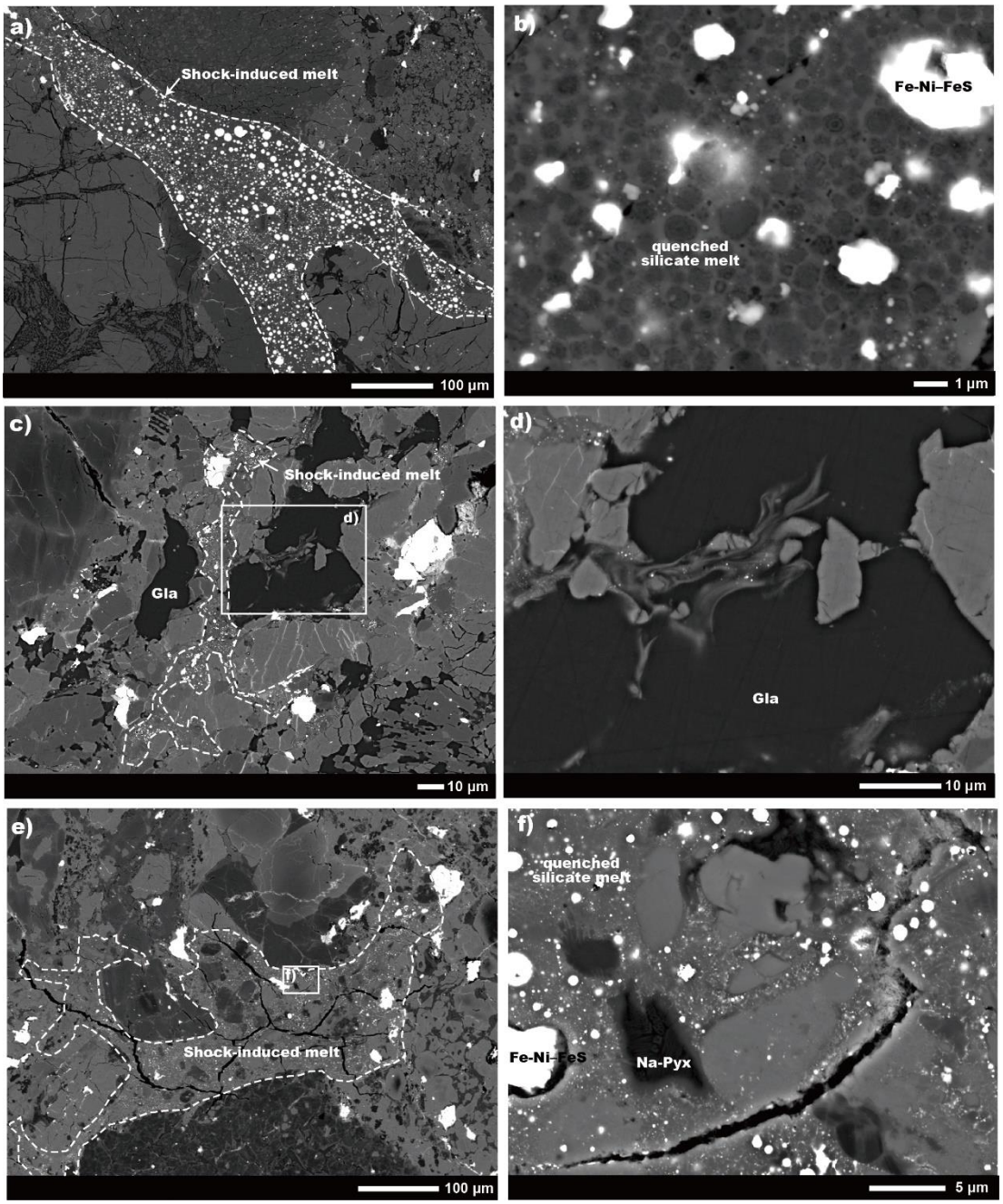

665

666 **Figure 5**. BSE images showing shock-induced melts in petrologic type 3 ordinary
667 chondrites. a) Pocket type melt in the Aba Panu L3 chondrite. b) High-magnification
668 image of shock-induced melt in a), c) Pocket type melt in A-87170 L3 chondrite, d)
669 High-magnification image of a white-colored box in c). A flow-like texture appears
670 in chondrule glasses, e) Pocket type melt in NWA 8664 L3 chondrite. f)
671 High-magnification image of a white-colored box in e). Na-pyx: Na-pyroxene.
672 Fe-Ni: metallic Fe-Ni, FeS: iron-sulfide.

673

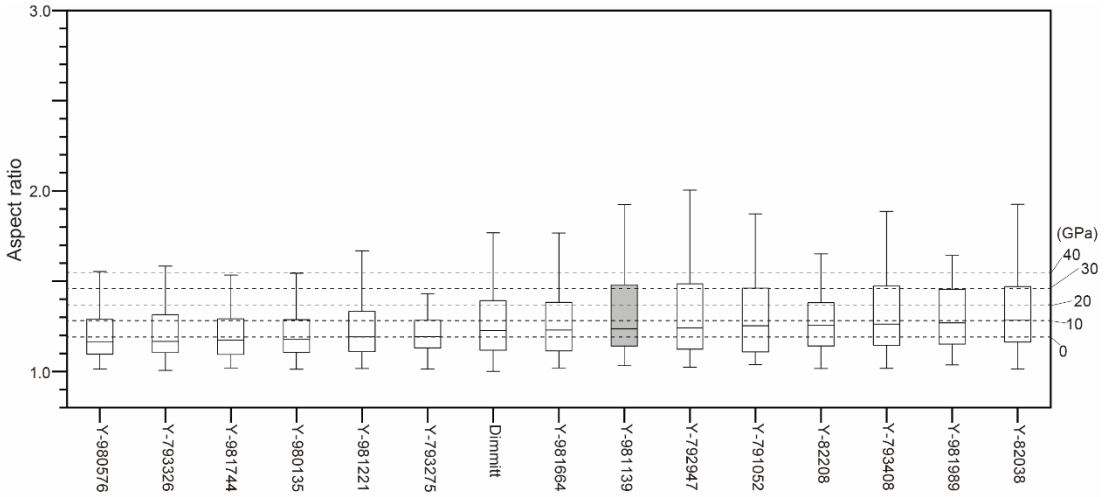

674

675 **Figure 6**. Box plots showing the aspect ratios of individual H3 ordinary chondrites.
676 The H3 ordinary chondrites are sorted according to the aspect ratios. White-colored
677 and gray-colored boxes are H3 ordinary chondrites without melts and those with
678 melts, respectively. Dashed lines correspond to each shock pressure estimated from
679 the shock experiments of ALH-78084 H3 chondrite.

680

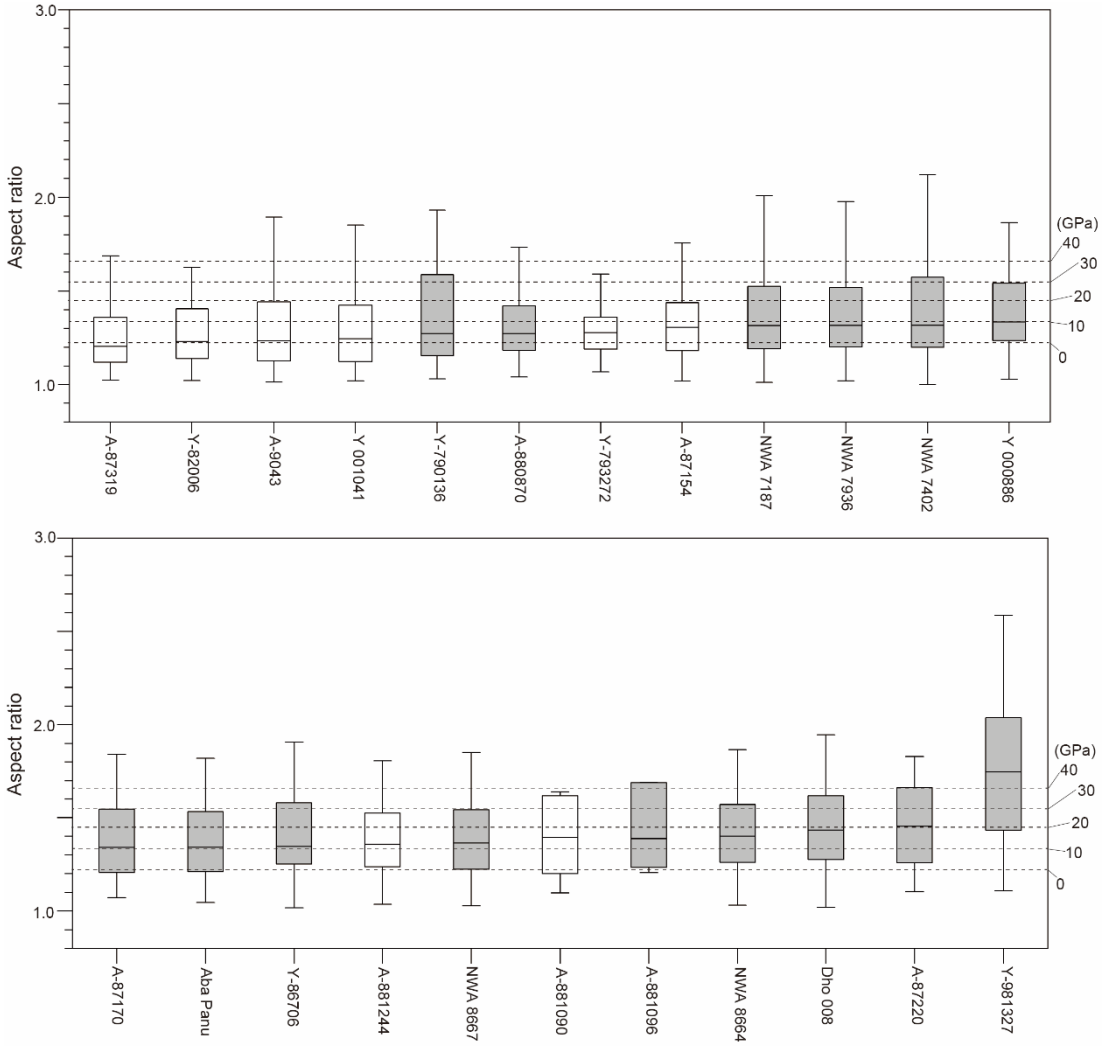

Figure 7. Box plots showing the aspect ratios of individual L3 ordinary chondrites. The L3 ordinary chondrites are sorted according to the aspect ratios. White-colored and gray-colored boxes are L3 ordinary chondrites without melts and those with melts, respectively. Dashed lines correspond to each shock pressure estimated from the shock experiments of Y-793375 L3 chondrite.

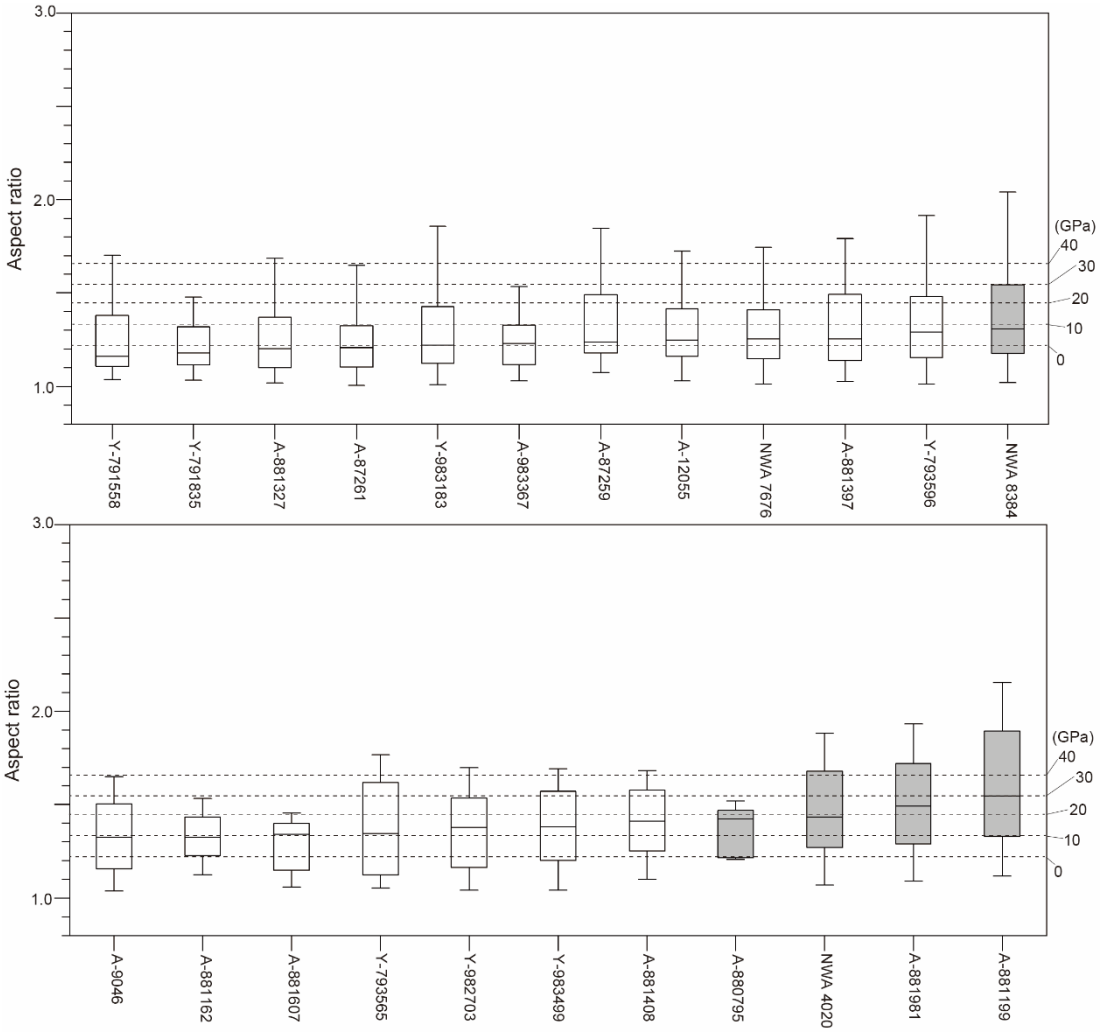

Figure 8. Box plots showing the aspect ratios of individual LL3 chondrites. The LL3 ordinary chondrites are sorted according to the aspect ratios. White-colored and gray-colored boxes are LL3 ordinary chondrites without melts and those with melts, respectively. Dashed lines correspond to each shock pressure estimated from the shock experiments of Y-793375 L3 chondrite.

694 Table 1. Run table for shock experiments.

	Shot No.	Target φ (mm)	Target Mass (g)	Target Thickness (mm)	Target Initial density (g/cm^3)	Flyer Material	Flyer Thickness (mm)	Impact velocity (km/s)	Equilibrium pressure (GPa)	Sample recovery
ALH-78084 H3	H_1	12	0.554	1.51	3.24	SUS	2	0.57	11.2	Three slices
	H_2	12	0.543	1.49	3.18	SUS	2	1.03	21.8	Three slices
	H_3	12	0.563	1.52	3.30	SUS	2	1.46	32.6	Three slices
	H_4	12	0.564	1.50	3.30	SUS	2	1.59	36.2	Three slices
	H_5	12	0.544	1.49	3.19	-	-	-	-	Broken during preparation
	H_6	12	0.551	1.50	3.23	W	2	1.40	42.9	Three slices
	H_7	6	-	1.50	-	SUS	2	1.17	25.1	One disc
Y-793375 L3	L_1	12	0.536	1.49	3.14	SUS	2	0.57	11.3	Three slices
	L_2	12	0.542	1.49	3.18	SUS	2	1.01	21.2	Three slices
	L_3	12	0.536	1.52	3.14	SUS	2	1.44	32.1	Three slices
	L_4	12	0.580	1.49	3.40	SUS	2	1.22	26.4	Three slices
	L_5	12	0.577	1.47	3.38	SUS	2	1.60	36.4	Three slices
	L_6	12	0.589	1.49	3.45	W	2	1.38	42.5	Three slices

695 SUS: SUS 304, W: Tungsten

696

697

698 Table 2. Data table for recovered samples.

	Shot No.	Shock pressure (GPa)	Long axis[#2] (μm)	Short axis[#2] (μm)	Aspect ratio[#2]	Number of analyses *n*	Length of open cracks (mm/mm^2)	Gini coefficients
ALH-78084 H3	H_0[#1]	0	429	352	1.19	258	-	0.33
	H_1	11.2	384	290	1.32	197	1.65	0.39
	H_2	21.8	414	273	1.38	162	0.93	0.46
	H_3	32.6	427	283	1.53	161	2.38	0.40
	H_4	36.2	389	254	1.46	187	4.17	0.41
	H_6	42.9	445	259	1.57	153	6.18	0.44
	H_7	25.1	-	-	-	-	-	-
Y-793375 L3	L_0[#1]	0	773	634	1.22	143	-	0.32
	L_1	11.3	707	506	1.36	89	2.19	0.25
	L_2	21.2	634	393	1.35	115	3.07	0.23
	L_3	32.1	749	482	1.47	79	5.42	0.27
	L_4	26.4	1296	770	1.61	36	5.31	0.31
	L_5	36.4	821	507	1.62	83	10.28	0.31
	L_6	42.5	711	426	1.75	77	8.74	0.49

699 #1 Shot No. H_0 and L_0 are starting materials. #2 median values. H_5 is removed because it is lost. -: No data

700